Proposal for High-Energy Cutoff Extension of Optical Harmonics of Solid Materials Using the Example of a One-Dimensional ZnO Crystal

Yue Lang, Zhaoyang Peng, Jinlei Liu, Zengxiu Zhao, and Shambhu Ghimire

Phys. Rev. Lett. **129**, 167402 — Published 12 October 2022
DOI: 10.1103/PhysRevLett.129.167402

Proposal for high-energy cutoff extension of optical harmonics of solid materials using the example of a one-dimensional ZnO crystal

Yue Lang,[1] Zhaoyang Peng,[1] Jinlei Liu,[1] Zengxiu Zhao,[1, *] and Shambhu Ghimire[2, †]
[1] *Department of Physics, National University of Defense Technology, Changsha, 410073, P.R. China*
[2] *Stanford PULSE Institute, SLAC National Accelerator Laboratory, Menlo Park, California, USA*
(Dated: September 15, 2022)

We propose a novel approach based on the sub-cycle injection of carriers to extend the high-energy cutoff in solid-state high-harmonics. The mechanism is firstly examined by employing the standard single-cell semiconductor Bloch equation (SC-SBE) method for one-dimensional (1D) Mathieu potential model for ZnO subjected to the intense linearly-polarized mid-infrared laser field and extreme-ultraviolet pulse. Then, we use coupled solution of Maxwell propagation equation and SC-SBE (MP-SBE) to propagate the fundamental laser field through the sample, and find that the high-harmonics pulse train from the entrance section of the sample can inject photon-carriers to the conduction bands with attosecond timing, subsequently leading to a dramatic extension of high-energy cutoff in harmonics from the backside. We predict that for a peak intensity at 2×10^{11} W/cm^2, as a result of the self-seeding, the high-energy cutoff shifts from 20th (7.75 eV) order to around 50th (19.38 eV) order harmonics.

High-harmonic spectra from gaseous targets are well-known to cover much of the extreme ultraviolet (EUV) wavelength range, making them suitable for generation of attosecond pulses [1–4]. In atomic media, the high-energy cutoff scales quadratically with the wavelength of the driving laser through the cutoff law: $\hbar\omega_{\mathrm{cutoff}} \sim I\lambda^2$ [5, 6]. Therefore, the use of long-wavelength lasers further extends the harmonic spectrum into the soft-x-ray wavelength range [7]. Recent realization of solid-state high harmonic generation (HHG) [8] and subsequent rapidly emerging activities [9, 10] indicate the possibility of a complementary approach to attosecond pulse metrology. Attributed to the novel microscopic generation mechanism [8, 11–17], solid-state HHG has shown unique features such as the ability to support stable EUV waveforms [18], ellipticity controlled harmonics [19], and higher efficiency because of the use of high density targets such as wide band dielectrics [20], van der Waals crystals [21], doped crystals [22] and topological materials [23, 24]. Particularly, high-energy cutoff scaling in solid-state HHG is markedly different to the atomic counterpart, for example, the cutoff scales linearly to the electric field, and driving wavelength dependence of solid-state HHG's high-energy cutoff depends on whether the underlying microscopic mechanism is dominated by intraband or interband channel [25]. Therefore, solid-state HHG calls for a new approach to extend its high-energy cutoff.

The generalized re-collision model [26] describes the solid-state HHG process using three semi-classical steps: (i) strong-field assisted tunneling of electrons from valence band to conduction band; (ii) acceleration of excited electrons and holes to high energies and momenta in their respective bands; and (iii) coherent recombination of electron hole pairs that produces high-energy photons. In the two-band model, the photon energy is limited by the maximal band gap. A secondary plateau can be produced through excitation to higher-lying conduction bands [21, 27–30] although the detailed tunneling mechanisms and particularly their temporal characteristics are yet to be studied. Here, we first consider theoretically a cascade process in a model solid, where we propagate a high-harmonic pulse with the fundamental laser field. We find optimal delays for various injecting harmonics where the pulse can excite photon-carriers to higher-lying conduction bands and extend the high-energy cutoff. More importantly, we verify that the previously generated high-harmonics in a real solid can participate in the latter nonlinear dynamics as it propagates with the fundamental field. We find a significant high-energy cutoff extension, from around 20th order to around 50th order, in harmonics emitted from the backside of the sample, which we understand by considering the carrier injection through self-seeding of harmonics.

The basic idea is depicted schematically in Fig. 1 by considering the solid subjected to both an infrared (IR) driving pulse and an EUV pulse. To simplify the analysis, the EUV pulse is confined to one cycle of the driving field as indicated by the purple line in Fig. 1(a). In the absence of EUV pulse, HHG can be understood as tunneling of electrons into the conduction band at t_1', and following excursion up to t_2' before final recombination at t_3', as illustrated in Fig. 1(b). Within the common framework of HHG in solids, most tunneling electrons locate near the minimal gap, i.e. Γ point ($\boldsymbol{k} = 0$), for direct band gap semiconductors. However, with the assistance of high frequency photons, it is possible for electrons with initial crystal momentum $\boldsymbol{k}_{\mathrm{EUV}}$ at t_1, depending on the energy of EUV photons, far from the center of Brillouin zone (BZ) to be driven to the minimal gap, then excited to the lowest conduction band C1 through one-photon absorption at t_2 (see Fig. 1(c) for an injection energy of the minimal gap), followed by excitation to the higher conduction band C2 under the influence of driving field through further Landau-Zener tunneling (LZT) [29] near the BZ edge at t_3 and final irradiation of higher frequency photons at t_4. The first and the second step can occur simultaneously under interaction with both the fundamental driving pulse and the EUV pulse. Other paths of UV photon involved HHG are found to contribute less significantly in the present study.

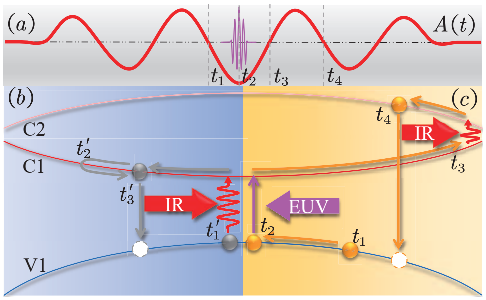

FIG. 1. (a) Vector potential of the incident IR (red) and EUV (purple) pulses. (b) Electron trajectory in conventional three step model for HHG in solids. (c) Electron trajectory in extended three-step model, i.e. acceleration of electrons initially locating far from Γ on highest valence band V1, transition assisted by one-photon absorption, acceleration on lowest conduction band C1, tunneling to higher conduction band C2 near the BZ boundary, acceleration, and recombination. t_n in (b) and (c) represents the moment marked in (a).

In order to examine this approach, we calculate the evolution of density matrix $\rho^{\boldsymbol{k}}_{mn}$ within the context of SC-SBE [31, 32]

$$\begin{aligned} i\dot{\rho}^{\boldsymbol{k}}_{mn}(t) = &\left[E^{\boldsymbol{k}'}_{m} - E^{\boldsymbol{k}'}_{n} - \frac{i\left(1-\delta_{mn}\right)}{T_2}\right]\rho^{\boldsymbol{k}}_{mn}(t) \\ &+\boldsymbol{F}(t)\cdot\sum_{l}\left[\boldsymbol{d}^{\boldsymbol{k}'}_{ml}\rho^{\boldsymbol{k}}_{ln}(t) - \boldsymbol{d}^{\boldsymbol{k}'}_{ln}\rho^{\boldsymbol{k}}_{ml}(t)\right], \qquad (1) \end{aligned}$$

where $E^{\boldsymbol{k}}_{m}$ is the mth band dispersion, $\boldsymbol{k}' = \boldsymbol{k} + \boldsymbol{A}(t)$ is the crystal momentum in the reciprocal frame moving with $\boldsymbol{A}(t) \equiv -\int^{t}\boldsymbol{F}(t')\,dt'$, $\boldsymbol{F}(t)$ is the electric field, T_2 is the empirical dephasing time, and $\boldsymbol{d}^{\boldsymbol{k}}_{mn}$ is the transitional dipole moments related to momentum transition moments (MTM) through canonical relation. $T_2 = \infty$ is used as an illustration and discussions on the impact of dephasing term are provided in supplementary materials (SM) [33]. Atomic units are used throughout unless otherwise stated. We use 1D Mathieu model potential [13, 32] $V(x) = -V_0\left[1+\cos\left(2\pi x/a_0\right)\right]$, with $V_0 = 0.37$, and $a_0 = 8$, to study HHG along Γ-M direction of zinc oxide (ZnO). The relatively simple 1D model would be a suitable approximation considering the computational load and our physical concern on the harmonic cutoff [36]. The ground state Bloch wave functions are reconstructed under the twisted parallel gauge to get smooth and periodic MTM in the first BZ [32], which resemble results employing tight-binding model [37]. As shown in Fig. 2(b), there are strong interband transitions between the highest valence band V1 and the lowest conduction band C1 near the Γ point and also between the two lowest conduction band, i.e. C1 and C2, near the BZ boundary.

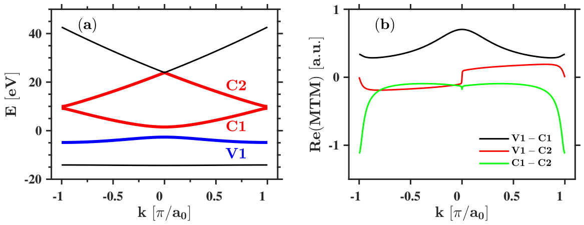

FIG. 2. (a) Band structure of model ZnO along Γ-M, where the three bands strongly coupled are highlighted, including the highest valence band V1 and two lowest conduction bands C1 and C2, to get an intuitive understanding of the extended three-step model in following analysis. (b) MTM between each pair of highlighted bands. Only real values are presented since 1D real and symmetric potential results in real $\boldsymbol{p}^{\boldsymbol{k}}_{mn}$ values. Note that the Fermi energy has been reset to 0 eV and two valence bands and three bands are used in simulation to get converged results.

The induced current is obtained by $\boldsymbol{J}(t) = -\int_{BZ} d\boldsymbol{k}\sum_{m\neq n}\rho^{\boldsymbol{k}}_{mn}\boldsymbol{p}^{\boldsymbol{k}+\boldsymbol{A}(t)}_{nm} - \int_{BZ} d\boldsymbol{k}\sum_{m}\rho^{\boldsymbol{k}}_{mm}\boldsymbol{p}^{\boldsymbol{k}+\boldsymbol{A}(t)}_{mm}$. The first and second terms on the right-hand side are commonly referred to as the interband and intraband currents, respectively. Note that contributions from all Bloch states in the BZ have been shown to contribute to solid HHG [36, 38]. The linearly polarized pulse is centered at 3200 nm ($\omega_L = 0.39$ eV) with a peak intensity of $I_L = 2\times10^{11}$ W/cm^2, a duration of 4 cycles, and a cosine square envelope. As an illustration, the injection ultraviolet (UV) pulse has the same pulse shape with an intensity of 2×10^{7} W/cm^2 and a wavelength of 291 nm ($11\omega_L$, the minimal gap energy). The spectrum is obtained by Fourier transformation of the first derivative of the total current (see SM [33]). Results on other injection wavelengths and simulation details are presented in SM [33]. Two cases with time-delays between the two pulses, 0 and $\frac{1}{4}T_L$ (referred to as case 1 and 2, respectively), are considered as indicated in Fig. 3(a), where T_L is the optical period at 3200 nm. As seen in Fig. 3(b), with the injection of UV pulse at delay of $\frac{1}{4}T_L$, a significant population of electrons on the valence band is excited to the conduction band through one-photon absorption, which contributes to the enhancement of HHG near the minimal gap (from $11\omega_L$ to around $15\omega_L$). Compared to case 1, nearly two orders of enhancement of HHG around $50\omega_L$ clearly illustrates that proper injection of UV can significantly increase the cutoff.

The underlying dynamics can be understood by examining the evolution of carrier population. In Fig. 4, we show population differences between schemes under the IR+UV pulse and under the IR pulse, i.e. $\mathrm{N}^{b}_{\mathrm{IR+UV}}(t) - \mathrm{N}^{b}_{\mathrm{IR}}(t)$, where b is the band indice. As shown in the left column for case 1, a significant population with initial

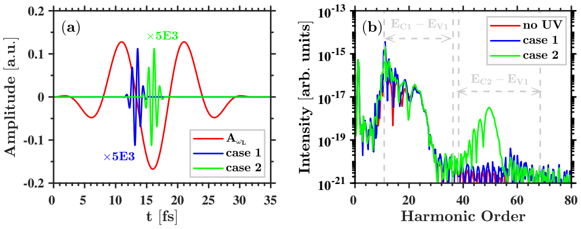

FIG. 3. (a) Temporal profiles of the driving IR field (red) and the injecting UV pulse at 0 (blue, referred to as case 1) and $\frac{1}{4}T_L$ delay (green, case 2). Note the UV pulse is injected at the zero-crossing (negative maximum) of the vector potential of the IR pulse for case 1 (case 2). The field amplitudes have been scaled up separately. (b) HHG spectra for IR only (red), case 1 (blue) and case 2 (green). Dashed lines mark the minimal and maximal gaps between V1 and C1, and V1 and C2.

$k \approx 0$ is excited to the lowest conduction band C1 at the instant of UV injection ($t \approx 13$ fs) through one-photon absorption. The curving stripes demonstrate intraband acceleration driven by the IR field. A certain amount of additionally injected electrons still populates on C1 after the end of IR pulse. For case 2, it is clearly illustrated that the one-photon excited electrons initially locate at $k \approx 0.7\pi/a_0$. These electrons are firstly driven on V1 by IR field and reach the Γ point at the instant of UV injection, where they are excited to C1 through one-photon absorption, as shown in Fig. 4 (b2) and (c2). Then, under the acceleration of IR field, they are driven to the BZ boundary on C1, followed by further transition to higher band C2 through LZT at the next appropriate strength of electric field, i.e. 23 fs in this case. Though other electrons at initial crystal momenta between 0.1 and $0.7\pi/a_0$ can be excited to C1, they fail to transit to higher conduction band C2 due to the low strength of electric field at the instant of approaching the BZ boundary. In addition, comparison between time frequency spectrum and the real space trajectories of electrons and holes predicted by acceleration theorem can also solidify this model (see Fig. S1 in SM [33]). Additional simulations illustrate that harmonic intensity in the second plateau scales linearly with the intensity of injection UV pulse, which further indicate that electrons populating on C2 are initially excited to C1 through one photon absorption. The optimal delay is found at $\frac{1}{4}T_L$ for the injection energy of $11\hbar\omega_L$. However, with the increasing of injection photon energy, the optimal delay varies and the delay sensitivity is weaken (see Fig. S2 in SM [33]). In other words, when broad-bandwidth UV pulse is injected, it is unnecessary to precisely control the delay for cutoff extension. Note that the present two-pulse scheme differs from previous studies on gas [39] and solids [40]. Also, injection pulse distinguishes our scheme from the 4-step model [41].

We then investigate the possibility of self-seeding of photon-carriers into the higher conduction band C2. We

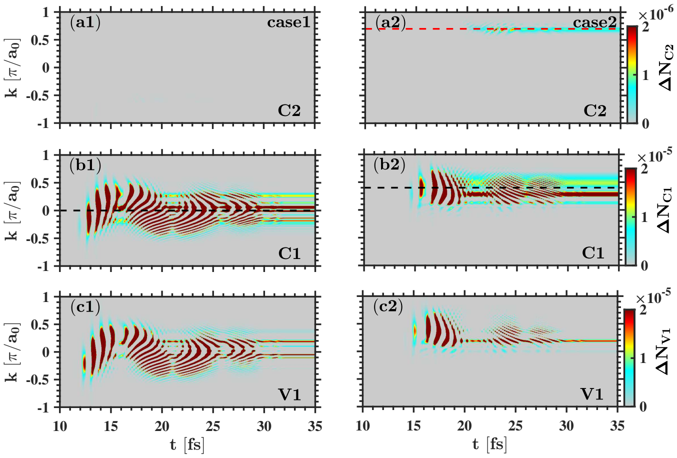

FIG. 4. Evolution of the carrier population growth on different bands for case 1 (left) and case 2 (right), relative to the case when only the IR field is presented. The red and black dashed lines show the central crystal momentum of excited carriers on C2 and C1, respectively.

closely follow Refs. [42, 43], where the propagation can be considered by coupled solution of Eq. (1) and the Maxwell propagation equation

$$\frac{1}{c^2}\frac{\partial^2}{\partial t^2}\boldsymbol{A}(t) - \nabla_{\boldsymbol{r}}^2 \boldsymbol{A}(t) = \mu_0 \boldsymbol{J}(t), \tag{2}$$

with $\boldsymbol{A}$ the vector potential, μ_0 the magnetic permeability in vacuum and $\boldsymbol{J}$ the local current calculated by SC-SBE, respectively. In the case of normal incidence of linearly-polarized pulse, Eq. (2) reduces to the 1D form to be solved in this research (see SM [33] for more details). It should be noted that, based on the known optical properties of ZnO such as the refractive index n, a scale factor for $\boldsymbol{J}$ should be multiplied to account for the reduced dimensionality [44]. Parameters of the initial pulse remains the same with the fundamental field used in the single-cell illustration except that the duration has been increased to 7 cycles.

The main results of HHG from a 20 μm-thick target are shown in Fig. 5(a). The reflected spectrum (blue line) resembles that from SC-SBE (black line). In contrast, the transmitted spectrum (red line) clearly indicates that it undergoes a nonlinear enhancement in the first plateau and a significant extension of the spectral range. The nonlinear gain can be predicted by the competition between absorption and phase matching during propagation [45]. Evolution of the yield of the nth harmonic $Y_n = \int_{(n-0.5)\omega_L}^{(n+0.5)\omega_L} I(\omega)\, d\omega$ with propagation length can be predicted by phase matching model $Y_n(z) \propto \frac{L_{\text{abs}}^2}{1+4\pi^2\left(\frac{L_{\text{abs}}}{L_{\text{coh}}}\right)^2} \times \left[1 + e^{-\frac{z}{L_{\text{abs}}}} - 2\cos\left(\frac{\pi z}{L_{\text{coh}}}\right) e^{-\frac{z}{2L_{\text{abs}}}}\right]$ (see SM [33]), where the absorption length L_{abs} and coherence length L_{coh} can be estimated using linear response theory. It indicates that the propagation induced non-

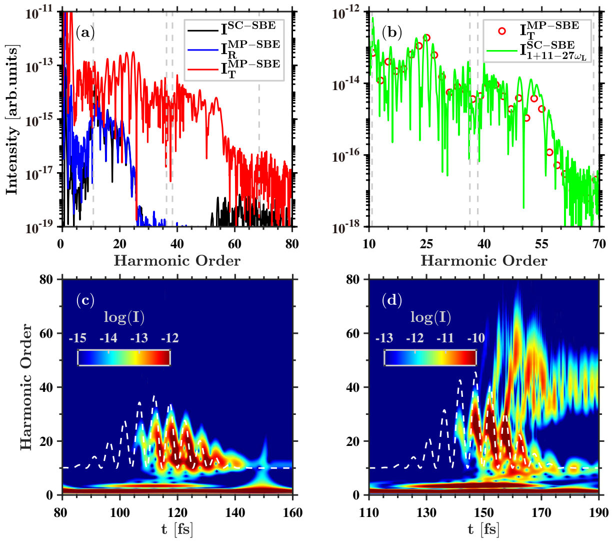

FIG. 5. (a) Emission spectra from SC-SBE (black solid line), reflected (blue solid line) and transmitted (red solid line) emissions by MP-SBE, respectively. (b) Emission spectra from a single cell subjected to the fundamental pulse and additional components of $11-27\omega_L$ harmonics (green solid line). Averaged intensity of odd harmonics in the forward radiation (red circles) is plotted as a guide to the eye. Dotted lines in (a) and (b) depict the minimal and maximal energy difference between the two lowest conduction bands and the highest valence band. Time-frequency spectrogram of backward (c) and forward (d) field in logarithmic scale. The square of the vector field potential A is illustrated in white dashed lines.

linear gain at the exit side is proportional to the square of absorption length, i.e. $G_n = \frac{I_n}{\widetilde{P}_n^2} \propto (L_{\rm abs})^2$. Therefore, compared to SC-SBE, the transmitted radiation in MP-SBE undergoes nonlinear gain G_n, which results in a stronger signal for higher frequency between $11\omega_L$ and $25\omega_L$ in Fig. 5(a) (see red and blue solid lines) because of larger $L_{\rm abs}$ for higher frequencies in this region.

To verify the role of harmonics in electron dynamics, we perform a SC-SBE calculation with the interacting field taken as the superposition of the fundamental frequency and a range of high-harmonics (see SM [33]). As shown in Fig. 5(b), when the additional pulse composed of $11\omega_L$ to $27\omega_L$ harmonics experienced by the last cell before exit is applied, the generated spectrum reproduces the transmitted emission. Minor difference in the details, especially from $40\omega_L$ to $60\omega_L$, can be attributed to interference among radiation from electron hole pairs excited at different k points in the BZ, since electrons in the whole BZ are considered in our simulation to contribute to the current. The deep minimum in the spectra can be understood by the destructive interference from different excited Bloch states under the condition of broad-bandwidth injection. The agreement between the spectra confirms that self-injection harmonics play a crucial role in the amplification and in the extension of high-energy cutoff. In addition, we show the time frequency profiles of the reflected and transmitted harmonics in Fig. 5(c) and (d) respectively through continuous wavelet transform (see SM [33]). In the transmitted harmonics, the harmonic pulse train injects the population to higher bands at different times within sub-cycle of the fundamental driving pulse due to their intrinsic chirp. Similar sub-cycle chirp has been observed experimentally in the emission phase of harmonics in the primary and secondary plateau [28]. As being pointed out formerly, the injection of broad-bandwidth harmonics during propagation wipes out the sensitivity on delay for certain harmonic injection. Therefore the self-injection induced cutoff extension can be general in the sense that it does not depend critically on the delay. We note that dephasing of electronic coherence is not introduced in this work which leads to unrealistic residual radiation through free induction decay.

The concept of propagation-induced injection of carriers is further tested and solidified by employing band dispersion and MTM from VASP [46] for magnesium oxide (see Fig. S10 in SM [33]). Together with simulations with varying incident intensities and wavelengths, the results indicate that longer wavelengths and materials with small band gap between conduction bands near the BZ boundary benefit the production of high energy photons as well as shorter attosecond pulses. The basic idea of EUV initiated self-seeding of HHG to extend high-energy cutoff has been investigated in gaseous media [39]. Our calculations indicate that extending those ideas to solid-state HHG requires a careful consideration of propagation effects. Moreover, we find that, by changing the sample thickness from 50 μm to 10 μm, the relative efficiency of the secondary plateau increases dramatically by many orders of magnitude (see Fig. S8 in SM [33]). In experiments, it might be difficult to obtain desired thickness, certainly in a wide range of materials, so one could use two targets: the first for the generation of UV seed, and the second for high-energy cutoff extension to the EUV wavelength range. We note that secondary plateau has been reported even in an one sample configuration using solid Argon and solid Krypton, where the sample thickness can be varied in situ[21].

In conclusion, we proposed a novel method to extend high-energy cutoff for solid-state HHG based on the subcycle carrier injection. Combing semiconductor Bloch equation with Maxwell propagation equation, we demonstrated the important role of the generated harmonics in participating electron dynamics during propagation in solids. It is found that the self-seeding of harmonics can inject additional carriers into the conduction bands and thus leads to the nonlinear gain and cutoff extension of harmonics which is generally absent for HHG from atomic gases. These findings advance our understanding of the novel HHG process in solid materials including the origin of secondary plateau, which is a unique feature recently identified in experiments. We also find theoretically that the reflected harmonics can provide a good reference because they avoid much of the propagation effects.

The work at National University of Defense Technology is supported by the Major Research plan of NSF of China (Grant No. 91850201), China National Key R&D Program (Grant No. 2019YFA0307703) and the NSF of China(Grant No. 12234020, 12274461 and 11904400). The work at SLAC is supported by the US Department of Energy, Office of Science, Basic Energy Sciences, Chemical Sciences, Geosciences, and Biosciences Division through the AMOS program.

---

* zhaozengxiu@nudt.edu.cn
† shambhu@slac.stanford.edu

[1] E. Goulielmakis, M. Schultze, M. Hofstetter, V. S. Yakovlev, J. Gagnon, M. Uiberacker, A. L. Aquila, E. M. Gullikson, D. T. Attwood, R. Kienberger, F. Krausz, and U. Kleineberg, Science **320**, 1614 (2008).
[2] T. Popmintchev, M.-C. Chen, D. Popmintchev, P. Arpin, S. Brown, S. Ališauskas, G. Andriukaitis, T. Balčiunas, O. D. Mücke, A. Pugzlys, A. Baltuška, B. Shim, S. E. Schrauth, A. Gaeta, C. Hernández-García, L. Plaja, A. Becker, A. Jaron-Becker, M. M. Murnane, and H. C. Kapteyn, Science **336**, 1287 (2012).
[3] J. Henkel, T. Witting, D. Fabris, M. Lein, P. L. Knight, J. W. G. Tisch, and J. P. Marangos, Physical Review A **87**, 043818 (2013).
[4] J. Li, J. Lu, A. Chew, S. Han, J. Li, Y. Wu, H. Wang, S. Ghimire, and Z. Chang, Nature Communications **11**, 2748 (2020).
[5] K. J. Schafer, B. Yang, L. F. DiMauro, and K. C. Kulander, Physical Review Letters **70**, 1599 (1993).
[6] P. B. Corkum, Physical Review Letters **71**, 1994 (1993).
[7] B. Shan and Z. Chang, Phys. Rev. A **65**, 011804 (2001).
[8] S. Ghimire, A. D. Dichiara, E. Sistrunk, P. Agostini, L. F. Dimauro, and D. A. Reis, Nature Physics **7**, 138 (2011).
[9] S. Ghimire and D. A. Reis, Nature Physics **15**, 10 (2019).
[10] U. Huttner, M. Kira, and S. W. Koch, Laser & Photonics Reviews **11**, 1700049 (2017).
[11] D. Golde, T. Meier, and S. W. Koch, Physical Review B **77**, 075330 (2008).
[12] S. Ghimire, A. D. DiChiara, E. Sistrunk, G. Ndabashimiye, U. B. Szafruga, A. Mohammad, P. Agostini, L. F. DiMauro, and D. A. Reis, Physical Review A **85**, 043836 (2012).
[13] M. Wu, S. Ghimire, D. A. Reis, K. J. Schafer, and M. B. Gaarde, Physical Review A **91**, 043839 (2015).
[14] G. Vampa, C. R. McDonald, G. Orlando, P. B. Corkum, and T. Brabec, Physical Review B **91**, 064302 (2015).
[15] N. Tancogne-Dejean, O. D. Mücke, F. X. Kärtner, and A. Rubio, Physical Review Letters **118**, 87403 (2017).
[16] L. Yue and M. B. Gaarde, Journal of the Optical Society of America B **39**, 535 (2022).
[17] L. Li, P. Lan, X. Zhu, and P. Lu, Physical Review Letters **127**, 223201 (2021).
[18] M. Garg, H. Y. Kim, and E. Goulielmakis, Nature Photonics **12**, 291 (2018).
[19] T. T. Luu and H. J. Wörner, The European Physical Journal Special Topics **230**, 4057 (2021).
[20] T. T. Luu, M. Garg, S. Yu. Kruchinin, A. Moulet, M. T. Hassan, and E. Goulielmakis, Nature **521**, 498 (2015).
[21] G. Ndabashimiye, S. Ghimire, M. Wu, D. A. Browne, K. J. Schafer, M. B. Gaarde, and D. A. Reis, Nature **534**, 520 (2016).
[22] V. E. Nefedova, S. Fröhlich, F. Navarrete, N. Tancogne-Dejean, D. Franz, A. Hamdou, S. Kaassamani, D. Gauthier, R. Nicolas, G. Jargot, M. Hanna, P. Georges, M. F. Ciappina, U. Thumm, W. Boutu, and H. Merdji, Applied Physics Letters **118**, 201103 (2021).
[23] H. Drüeke and D. Bauer, Physical Review A **99**, 053402 (2019).
[24] D. Bauer and K. K. Hansen, Physical Review Letters **120**, 177401 (2018).
[25] X. Liu, X. Zhu, X. Zhang, D. Wang, P. Lan, and P. Lu, Optics Express **25**, 29216 (2017).
[26] G. Vampa, T. J. Hammond, N. Thiré, B. E. Schmidt, F. Légaré, C. R. McDonald, T. Brabec, D. D. Klug, and P. B. Corkum, Physical Review Letters **115**, 193603 (2015).
[27] M. Wu, D. A. Browne, K. J. Schafer, and M. B. Gaarde, Phys. Rev. A **94**, 063403 (2016).
[28] Y. S. You, M. Wu, Y. Yin, A. Chew, X. Ren, S. Gholam-Mirzaei, D. A. Browne, M. Chini, Z. Chang, K. J. Schafer, M. B. Gaarde, and S. Ghimire, Optics Letters **42**, 1816 (2017).
[29] A. J. Uzan, G. Orenstein, Á. Jiménez-Galán, C. McDonald, R. E. Silva, B. D. Bruner, N. D. Klimkin, V. Blanchet, T. Arusi-Parpar, M. Krüger, A. N. Rubtsov, O. Smirnova, M. Ivanov, B. Yan, T. Brabec, and N. Dudovich, Nature Photonics **14**, 183 (2020).
[30] A. J. Uzan-Narovlansky, Á. Jiménez-Galán, G. Orenstein, R. E. F. Silva, T. Arusi-Parpar, S. Shames, B. D. Bruner, B. Yan, O. Smirnova, M. Ivanov, and N. Dudovich, Nature Photonics **16**, 428 (2022).
[31] I. Floss, C. Lemell, G. Wachter, V. Smejkal, S. A. Sato, X. M. Tong, K. Yabana, and J. Burgdörfer, Physical Review A **97**, 011401 (2018).
[32] L. Yue and M. B. Gaarde, Physical Review A **101**, 053411 (2020).
[33] See Supplementary Material https://link.aps.org/supplemental/ for details of the theoretical methods and simulation results, which includes Ref. [34-35].
[34] U. Lindefelt, H. E. Nilsson, and M. Hjelm, Semiconductor Science and Technology **19**, 1061 (2004) .
[35] I. Kilen, M. Kolesik, J. Hader, J. V. Moloney, U. Huttner, M. K. Hagen, and S. W. Koch, Physical Review Letters **125**, 83901 (2020).
[36] F. Navarrete, M. F. Ciappina, and U. Thumm, Physical Review A **100**, 033405 (2019).
[37] S. Jiang, J. Chen, H. Wei, C. Yu, R. Lu, and C. D. Lin, Physical Review Letters **120**, 253201 (2018).
[38] C. Yu, H. Iravani, and L. B. Madsen, Physical Review A **102**, 033105 (2020).
[39] M. Krüger, D. Azoury, B. Bruner, and N. Dudovich, Applied Sciences **9**, 378 (2019).

[40] F. Navarrete and U. Thumm, Physical Review A **102**, 063123 (2020).

[41] L. Li, P. Lan, X. Zhu, T. Huang, Q. Zhang, M. Lein, and P. Lu, Physical Review Letters **122**, 193901 (2019).

[42] K. Yabana, T. Sugiyama, Y. Shinohara, T. Otobe, and G. F. Bertsch, Physical Review B **85**, 045134 (2012).

[43] A. Yamada and K. Yabana, Physical Review B **99**, 245103 (2019).

[44] M. Korbman, S. Yu Kruchinin, and V. S. Yakovlev, New Journal of Physics **15**, 013006 (2013).

[45] Z. Chang, *Fundamentals of Attosecond Optics*, 1st ed. (CRC Press, Boca Raton, 2011).

[46] S. Jiang, C. Yu, J. Chen, Y. Huang, R. Lu, and C. D. Lin, Physical Review B **102**, 155201 (2020)
.